

Molecular Imaging of Vulnerable Atherosclerotic Plaques *in Vivo* with Osteopontin-Specific Upconversion Nanoprobes

Ruirui Qiao,^{†,‡} Hongyu Qiao,^{‡,§,‡} Yan Zhang,[‡] Yabin Wang,[‡] Chongwei Chi,^{||} Jie Tian,^{||} Lifang Zhang,[†] Feng Cao,^{*,‡} and Mingyuan Gao^{*,†,||}

[†]Institute of Chemistry, Chinese Academy of Sciences, Bei Yi Jie 2, Zhong Guan Cun, Beijing 100190, P. R. China

[‡]Department of Cardiology, Chinese PLA General Hospital, No. 28 Fuxing Road, Beijing 100853, P. R. China

[§]Department of Cardiology, Xijing Hospital, Fourth Military Medical University, Xi'an 710032, P. R. China

^{||}Key Laboratory of Molecular Imaging, Chinese Academy of Sciences, No. 95 Zhong Guan Cun East Road, Beijing 100190, P. R. China

ABSTRACT: Owing to the high mortality rate of cardiovascular diseases, developing novel noninvasive diagnostic methods becomes urgent and mandatory. It is well-known that the rupture of vulnerable plaques directly leads to deadly consequences. However, differentiating vulnerable plaques from stable plaques remains challenging in the clinic. In the current study, osteopontin (OPN), a secreted biomarker associated with macrophages and foamy macrophages, was selected as a target for identifying the vulnerable plaques. A dual modality imaging probe was constructed by covalently attaching an OPN antibody to NaGdF₄:Yb,Er@NaGdF₄ upconversion nanoparticles. Upon intravenous injection of the resulting probes, upconversion optical imaging was performed to visualize the plaques induced by altering the shear stress in carotid arteries of a mouse model. The imaging studies revealed that the signals of vulnerable and stable plaques induced by lowered shear stress and oscillatory shear stress, respectively, presented significantly different signal intensities, implying that the current probe and imaging strategy are potentially useful for a precise diagnosis of atherosclerosis plaques.

KEYWORDS: vulnerable plaques, macrophage, OPN, molecular imaging, upconversion nanoparticle



Cardiovascular diseases are one of the leading causes of deaths globally, which on average accounts for one death every 40 s and claims more lives each year than cancer.¹ According to the report of “Chinese Cardiovascular Disease in 2013”, approximately 290 million patients suffered from cardiovascular diseases, which amounted to 41.4% of the total deaths occurring in a city and 38.7% in a countryside. Atherosclerosis, a the major component of cardiovascular disease, is characterized by thickening and hardening of the arteries arising from maladaptive inflammatory responses, dysregulated lipid metabolism, and plaque build-up.² Atherosclerosis’ clinical complications such as stroke, myocardial infarction, and so on account for 48% of noncommunicable diseases’ mortality in the world.³

There could be decades before symptoms occurring in atherosclerosis patients and sometimes sudden death resulting from acute cardiovascular diseases could happen without any warning.¹ It has been demonstrated in clinical studies that more than 50% of patients afflicted with coronary atherosclerosis

present sudden death or myocardial infarction as their first clinical manifestation,⁴ whereas approximately two-thirds of acute coronary syndromes occur in patients who are often diagnosed as having intermediate risks with traditional risk-stratification methods, indicating an urgent need for evaluating the atherosclerosis diseases at their asymptomatic phase. Actually, the composition of atherosclerosis plaques is playing an important role in clinical events such as rupture, thrombosis, etc. Two major categories of plaques, *i.e.*, stable and vulnerable, are classified accordingly. Stable atherosclerosis plaques tend to be rich in extracellular matrices and smooth muscle cells, while vulnerable plaques are rich in certain macrophage subsets, *e.g.*, foamy macrophages and inflammatory cells. The most common and fatal atherosclerosis complications such as myocardial

Received: November 22, 2016

Accepted: January 25, 2017

Published: January 25, 2017

infarction or ischemic stroke are mostly caused by the rupture of vulnerable plaques.⁵

Currently, the clinical imaging approaches such as intravascular ultrasonography (IVUS), optical coherence tomography (OCT), X-ray computed tomography (CT), and magnetic resonance imaging (MRI) are widely employed for assessing the severity of atherosclerosis plaques. For example, CT is commonly applied for calcium scoring,⁵ whereas IVUS is used for intimal media thickness measurements. But these methods are not able to differentiate the type of atherosclerosis plaques from molecular level. However, high macrophage content in plaques has been identified as an important indicator of vulnerability with the progression of atherosclerosis plaques.⁶ A pathology study of vulnerable plaques from clinical samples revealed that the average number of macrophages in vulnerable plaques can be nearly 4-fold of those in stable plaques,^{7,8} indicating that macrophages are potential cellular targets for noninvasively differentiating vulnerable plaques from stable plaques. As a matter of fact, macrophages will be transformed into foamy macrophages upon overloading of lipid contents during the atherosclerosis progression. In this context, noninvasively detecting macrophages, especially foamy macrophages, may provide a promising approach for predicting the vulnerability of plaques, which is meaningful for developing more efficient theranostics.

Molecular imaging methods have been intensively investigated for visualizing and evaluating the atherosclerosis plaque status.^{5,9,10} Meanwhile, different molecular probes based on various nanomaterials have been developed for visualizing the inflammation processes associated with atherosclerosis progression.¹¹ Based on the phagocytosis of macrophages in plaques, several superparamagnetic nanoprobe have been reported for atherosclerosis plaque detection with MRI or dual-modality imaging approaches in animal models^{12–15} and patients.^{16–18} Probes based on the recognition of biomarkers such as VCAM-1 (vascular cell adhesion protein-1), $\alpha_v\beta_3$ integrin, scavenger receptors, ICAM-1 (intercellular adhesion molecule-1), and CCR-2 (chemokine (C–C motif) receptor 2) have also been developed, but not specifically for macrophages.¹⁹ Moreover, the probes and related imaging methods are suffering from low sensitivity.

Toward improved imaging sensitivity and specificity, herein we report a luminescent/magnetic rare-earth nanoprobe for visualizing vulnerable plaques. Due to the unique optical and intrinsic paramagnetic properties, Yb,Er-doped Gd-based nanoparticles, e.g., NaGdF₄:Yb,Er upconversion nanoparticles (UCNPs) have attracted extensive attention in tumor multimodality imaging and therapy.^{19–21} The upconversion luminescence is characterized by high photostability, multiwavelength emission, large anti-Stokes shift, and extremely weak background noise,²³ which is essentially useful for improving the imaging sensitivity *in vivo*.^{24,25} For example, we have previously demonstrated that the bioconjugates of antitumor antibody and PEGylated NaGdF₄:Yb,Er nanoparticles can be used for visualizing orthotopically transplanted tumors and their metastases and intraperitoneal tumors as well.^{20,26} Inspired by the relatively deep tissue penetration of the upconversion luminescence (3–5 cm),²⁷ a macrophage-specific molecular probe was constructed for imaging atherosclerosis through covalently conjugating a foamy macrophage-specific osteopontin (OPN) antibody to highly luminescent core@shell-type NaGdF₄:Yb,Er@NaGdF₄ nanoparticles, as OPN expression has a strong relation with macrophage and

foamy macrophage content, and plays a key role in the progression of vulnerable plaques including recruitment of leukocytes, increase of their viability, and induction of cytokine and MMP expression.^{28,29} Meanwhile, an animal model based on the alteration of shear stress in a carotid artery was constructed to simultaneously induce both stable and vulnerable plaques.³⁰ By combining *in vivo* imaging studies with *ex vivo* immunohistochemical analysis, we show that OPN is expressed more in vulnerable atherosclerotic plaques than in stable ones.

RESULTS AND DISCUSSION

Synthesis of NaGdF₄:Yb,Er@NaGdF₄ Nanocrystals. Codoping NaGdF₄ nanocrystals with Yb and Er leads to upconversion photoluminescence upon 980 nm excitation.²³ High luminescence brightness is of particular importance for the performance of the nanoprobe, especially the imaging sensitivity *in vivo*, while constructing a core@shell structure has widely been adopted for improving the luminescence intensity of the underlying core.²³ To maximize the contrast-enhancing performance of the nanocrystals for magnetic resonance imaging (MRI) while improving the luminescence intensity, in the current study, NaGdF₄ was chosen to overcoat NaGdF₄:Yb,Er nanocrystals to achieve high performance luminescent/magnetic bifunctional nanocrystals.²⁰ The results given in Figure 1a,b reveal that both core and core@shell particles are highly monodisperse with an average size of 12.4 ± 1.0 nm and 20.5 ± 0.8 nm, respectively. The powder X-ray diffraction (XRD) patterns in Figure 1c reveal that both core and core@shell particles are hexagonal nanocrystals. In addition, the average size of 18.3 nm for the core@shell particles, according to the Scherrer equation, is rather close to the TEM size, suggesting that the core@shell particles possess a high crystallinity degree, which is greatly in favor of eliminating the interfacial quenching sites between core and shell.³¹ Owing to the outstanding epitaxial growth of the shell, the luminescence intensity of the resulting core@shell nanocrystals, as shown in Figure 1d, is enhanced by a factor of 30.²²

Preparation of OPN-Specific Probes. For constructing OPN-specific probes, a ligand exchange process was performed for replacing the hydrophobic oleic acid ligand with a diphosphate polyethylene glycol (PEG) ligand to render the magnetic/upconversion nanocrystals water-soluble, biocompatible, and functionalizable. Although the luminescence intensity of the core nanocrystals was only increased by a factor of 30 through the NaGdF₄ shell coating, the luminescence intensity of the core was much better preserved after the particle surface PEGylation. As shown in Figure 2a, the luminescence enhancing factor was as high as 159 when comparing the PEGylated core@shell particles with the corresponding PEGylated cores, much higher than that previously reported for core and core@shell particles, showing an enhancing factor of 57 after being transferred into an aqueous system upon surface PEGylation.²⁰ In general, the luminescence intensity is inevitably decreased after the upconversion nanoparticles are transferred into an aqueous phase, due to the increased probability of nonradiative relaxation of the excited states involving different water vibrational modes.³¹ The remarkable retention effect of the shell coating on the upconversion luminescence reported herein can be attributed to the relatively thick shell in comparison with the previously reported particles, e.g., 8.1 nm vs 4.8 nm.³¹ Normally, the lowered upconversion emissions in aqueous systems are attributed to the strong

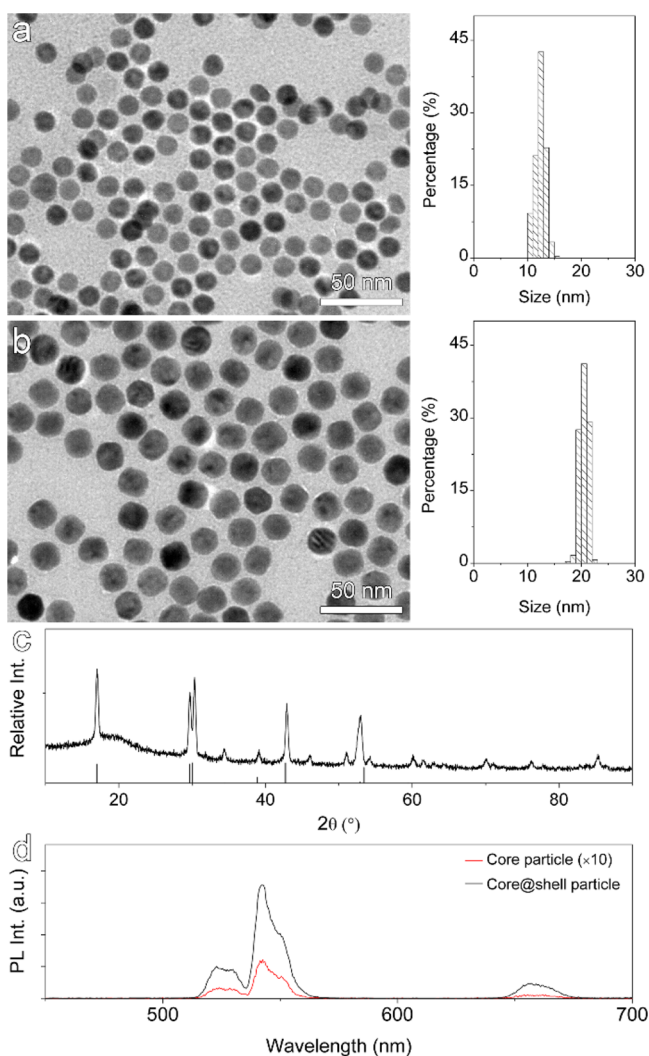


Figure 1. TEM images and size histograms of NaGdF₄:Yb,Er core (a) and NaGdF₄:Yb,Er@NaGdF₄ core@shell nanocrystals (b), together with their XRD patterns (c), and normalized upconversion luminescence spectra of these two types of nanocrystals in cyclohexane solutions recorded under 980 nm laser excitation (d). The vertical line pattern in (c) is drawn according to the standard data of hexagonal NaGdF₄ according to JCPDS card (no. 27-0699).

vibrational modes of the H₂O molecules ($\sim 3600\text{ cm}^{-1}$) that produce an increased nonradiative relaxation of the luminescent centers. The core@shell structure increases the distance between the luminescent centers and the vibrational modes and thus causes the nonradiative vibrational relaxation processes to be less efficient compared to the core sample.³²

Toward sensitive optical imaging, the PEGylated core@shell UCNP with optimized upconversion luminescence were chosen to build up OPN-specific probes for dual-modality imaging of atherosclerosis plaques. As it was previously discovered, OPN overexpressed by macrophages and foam cells is up-regulated in atherosclerosis plaques and promotes the adhesion, migration, and activation of macrophages.^{33–35} Based on the fact that normal macrophages and foamy macrophages are richer in vulnerable plaques than in stable plaques,²⁸ we assume that the OPN expression level is also higher in vulnerable plaques, which was also evidenced through our previous studies.³⁶ Therefore, an OPN-targeting probe

(UCNP-anti-OPN) was constructed for noninvasively distinguishing vulnerable atherosclerotic plaques from stable plaques *in vivo*. The conjugation between the PEGylated UCNP nanoparticles and anti-OPN antibody was realized through a “click” reaction between the maleimide moiety of particle surface PEG ligand and the thiol residues of partly reduced antibody.^{21,26} The dynamic light scattering results in Figure 2c reveal that no particle aggregation was induced by the conjugation reactions, and the hydrodynamic size of the UCNP is reasonably increased after surface attachment of the antibody molecules, while the polydispersed index (PDI) is slightly decreased from 0.359 for UCNP to 0.345 for UCNP-anti-OPN. Another evidence supporting the formation of the conjugates is that the particle surface zeta potential is slightly changed from $-2.33 \pm 0.20\text{ mV}$ to $0.29 \pm 2.17\text{ mV}$ after the conjugation reaction, as shown in Figure 2d, due to the fact that the isoelectric point of IgG typically locates in very weak base regions.

Cytotoxicity Evaluation of UCNP. Although a large number of studies support that gadolinium-based nanoparticles upon proper surface modification present a lower cytotoxicity than clinically used contrast agents such as Gd-DTPA,²¹ careful evaluations remain necessary, as the cytotoxicity is not only determined by the chemical composition of the particle core but also strongly associated with the surface physicochemical properties which largely govern the interactions between nanoparticles and cells. Therefore, the cytotoxicity of PEGylated UCNP was evaluated through cell viability, TUNEL apoptosis assay, and flow cytometry, respectively. As shown in Figure 3a, upon co-incubation with UCNP in a concentration range of 5–30 $\mu\text{g Gd/mL}$, Raw 264.7 cells do not show a significantly decreased viability over 24 h. In fact, the cytotoxicity of 20 nm PEGylated UCNP to GC7901 cells was previously studied, and the 50% inhibitory concentration (IC_{50}) value was determined to be around 13.8 mM for UCNP in terms of Gd³⁺ concentration, significantly higher than the maximum concentration used herein, *i.e.*, 30 $\mu\text{g Gd/mL}$ (0.19 mM Gd³⁺). The TUNEL experiment results, based on FITC staining of apoptotic cell nuclei as shown in Figure 3b, also support the low cytotoxicity of the PEGylated UCNP. The quantified data reveal that the apoptotic rate is slightly increased from $12.7 \pm 1.5\%$ for the control group to $14.6 \pm 1.1\%$ for UCNP group (30 $\mu\text{g Gd/mL}$) with $P > 0.05$, which is also supported by the flow cytometry results in Figure 3c. In brief, the above cytotoxicity studies based on three different types of methods indicate that the PEGylated core@shell UCNP for constructing OPN-specific nanoprobe possess a relatively safe profile.

In Vitro Foamy Macrophage Targeting of UCNP-Anti-OPN Nanoprobes. In the current study, an *in vitro* binding affinity assay was carried out to evaluate the OPN expression in macrophages by using a foamy macrophage model cell line, Raw 264.7 cells, after being exposed to oxidized low-density lipoprotein (Ox-LDL).³⁷ As displayed in Figure 4a, the macrophages stimulated with Ox-LDL present a much higher OPN expression level in the immunofluorescence assay, which is further confirmed through quantified analysis *via* Western blot assay. As given in Figure 4b, the OPN/ β -actin is 1.45 ± 0.21 for the stimulated macrophages, while that for the unstimulated ones is 0.62 ± 0.14 ($P < 0.05$). To further show the feasibility of using an UCNP-anti-OPN nanoprobe for targeting foamy macrophages, confocal upconversion microscopy was adopted to investigate the cell targeting ability of the

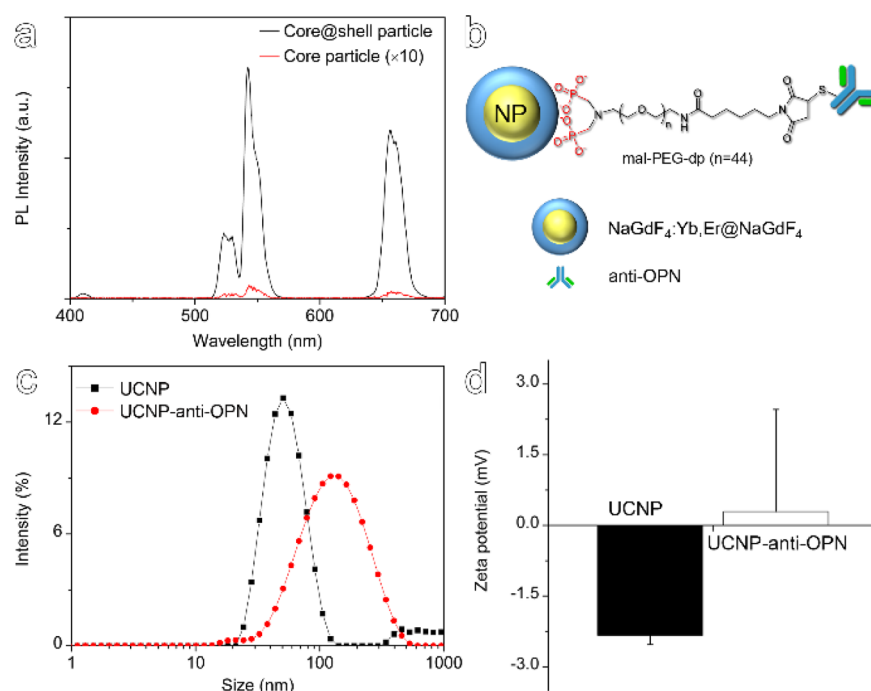


Figure 2. Normalized upconversion luminescence spectra of PEGylated core and core@shell particles in water recorded under 980 nm laser excitation (a), a schematic drawing of the UCNP-anti-OPN probe (b), hydrodynamic size distribution profiles (c), and zeta potential histogram (d) of UCNPs and UCNP-anti-OPN.

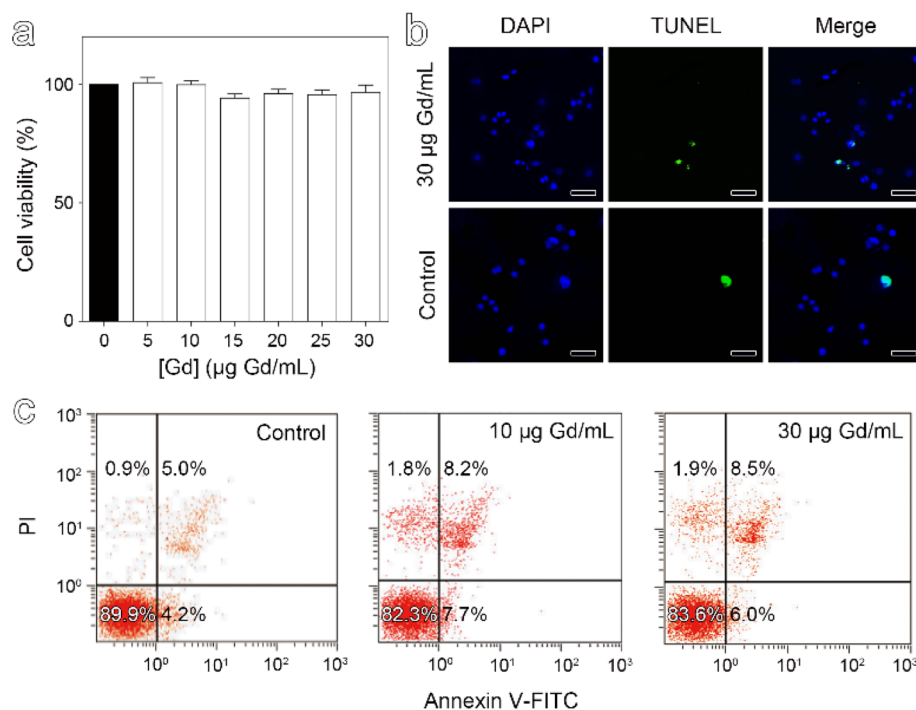


Figure 3. MTT (a), TUNEL (b), and flow cytometry (c) assays for evaluating the cytotoxicity of PEGylated UCNPs. The embedded scale bar in the microscopic images corresponds to 50 μm .

OPN-specific probe. As the $\text{NaGdF}_4:\text{Yb,Er}@/\text{NaGdF}_4$ nanoparticles present two distinguishable emissions with peak position located at around 542 and 656 nm, respectively, upon excitation at 980 nm, as shown in Figure 2a, a more reliable binding assay can be achieved through dual wavelength emissions. As shown in Figure 4c, the mother PEGylated UCNPs present rather weak nonspecific binding to normal macrophages, but this nonspecific adsorption is even weakened

for the stimulated macrophages, suggesting that Ox-LDL stimulation does not encourage the macrophage uptake of the PEGylated UCNPs. Most importantly, both normal macrophages and Ox-LDL stimulated macrophages present green and red emission signals remarkably consistent in space after incubating with the UCNP-anti-OPN probes, but different in intensity, while the macrophages co-incubated with excess OPN antibody apart from the UCNP-anti-OPN probes present

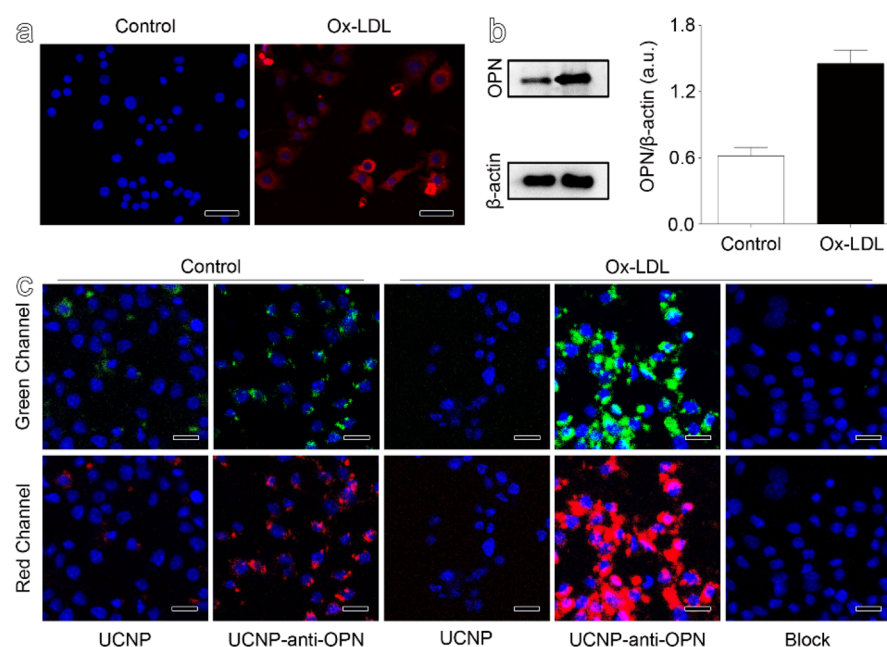


Figure 4. Confocal microscopy images of macrophages before (left) and after 24 h incubation with Ox-LDL (a), Western blot data for showing the expression of OPN/ β -actin in foamy macrophages upon Ox-LDL treatment ($*P < 0.05$ vs Control) (b), and upconversion microscopy images of Raw 264.7 macrophages (control) and Ox-LDL stimulated Raw 264.7 macrophages (Ox-LDL) obtained after incubation with UCNP, UCNP-anti-OPN, and excess OPN together with UCNP-anti-OPN probe (Block), respectively (c). The images were captured through both green and red channels, respectively, and then merged with nuclei staining images. The embedded scale bar in the microscopic images corresponds to 50 μ m.

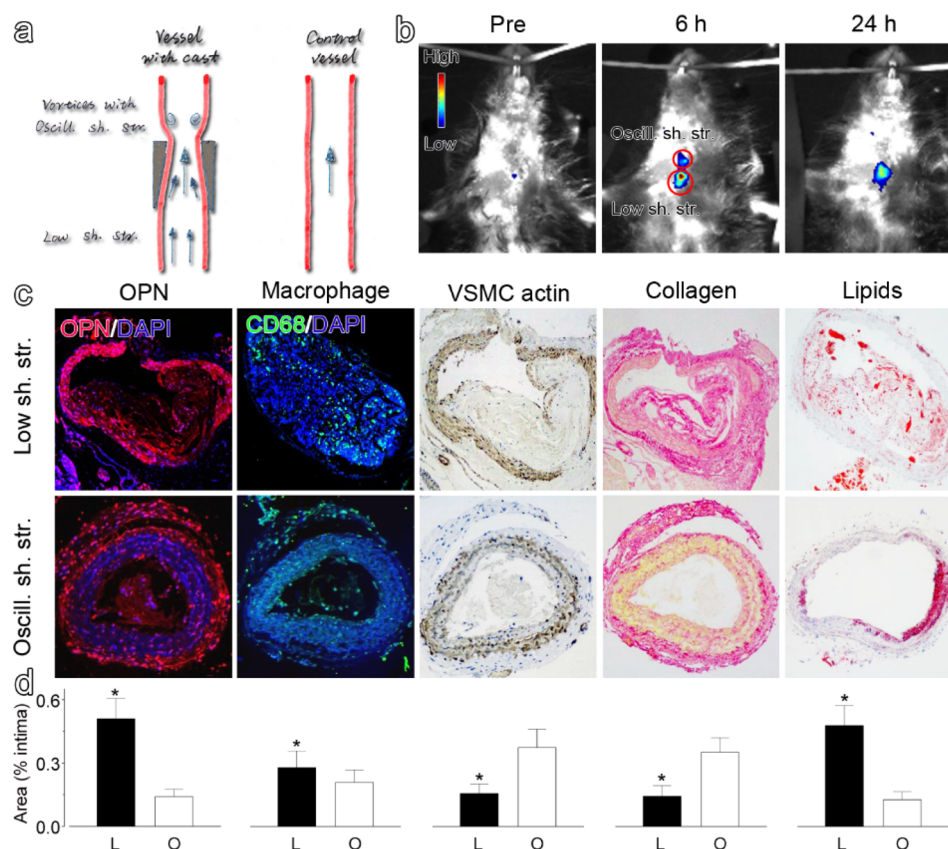


Figure 5. A schematic drawing for showing the varied stress-induced plaques in ApoE $^{-/-}$ mouse (a), *in vivo* upconversion luminescent images captured before and at different time points after intravenous injection of the UCNP-anti-OPN probe (the region of interest is encircled with red circles for showing the oscillatory shear stress (top) and lowered shear stress region (bottom) of the constrained vessel) (b), histological analyses (c), and quantified data of the different plaque regions upon various staining ($*P < 0.05$) (d).

nearly no signals. These experimental observations strongly suggest that the current probes exhibit excellent macrophage targeting ability through OPN, and the binding affinity is strongly correlated with the expression of OPN. Then through the different OPN expression levels between foamy macrophages and normal macrophages, targeted imaging of the former cells becomes possible.

In Vivo Optical/MR Imaging of Vulnerable Plaques.

Identification of vulnerable plaques remains a big challenge due to the limitations of clinical imaging techniques. For example, X-ray angiography is widely used for assessing atherosclerosis through luminal narrowing, however, atherosclerosis that does not encroach on the lumen is often omitted. Intravascular ultrasound, MRI, and three-dimensional carotid ultrasound do well in diagnosing plaques based on their morphology or tissue composition, but cannot distinguish the molecular signatures of rupture-prone plaques from those of stable ones. Indeed, more attention needs to be paid on emerging atherosclerosis imaging platforms that allow accurate visualization of culprit pathological processes than standard techniques and to develop these tools to help refine risk assessment models and to guide therapy.⁹ As a matter of fact, molecular imaging can, in principle, offer solutions for noninvasively visualizing the key molecules associated with the plaque vulnerability.

Macrophages have important roles in the progression of atherosclerosis and have been considered a promising target for detecting and characterizing atherosclerosis.^{38,39} Until now, most atherosclerotic plaque imaging studies rely on the uptake of nanoparticles, especially superparamagnetic iron oxide nanoparticles for MR imaging,^{18,40} as macrophages exhibit high endocytosis activity for nanomaterials.^{11,41} However, this approach may suffer from the following limitations: (1) conventional iron oxide nanoparticles as negative contrast agents reduce the contrast between iron oxide laden macrophages and blood;³⁹ and (2) iron oxide particle-labeled macrophages cannot be distinguished from other hypointense regions such as a hemorrhage and blood clots. Therefore, gadolinium-based nanoparticles as T_1 contrast agents become more suitable for atherosclerosis plaque diagnosis. Most importantly, specific targeting will increase the targeting efficacy by shortening the accumulation time of the probes at plaques and consequently improve the sensitivity for plaque detection.

For atherosclerosis plaque imaging, an animal model with vulnerable and stable atherosclerotic plaque phenotypes adjacent to each other along a single vessel was established with ApoE^{-/-} mice by altering the shear stress patterns of the carotid artery with a cast as previously described.^{42,43} As illustrated in Figure 5a, previous studies reveal that the upstream with lowered shear stress (low sh. str.) induced by the cast tends to form more vulnerable features, whereas the downstream with oscillatory shear stress (oscill. sh. str.) tends to form stable atherosclerotic plaques. Upon intravenous injection of the UCNP-anti-OPN probes, optical images were acquired at different time points post-injection. As shown in Figure 5b, two distinctive signals were detected through a 540 nm filter 6 h post-injection, perfectly consistent with the positions of the two plaques induced. However, the top signal disappeared, while the bottom one largely lost its signal intensity 24 h post-injection.

Histological studies were conducted right after the optical imaging studies. The results given in Figure 5c clearly reveal that the lowered shear stress region shows a much higher expression of OPN and slightly more accumulation of

macrophages through OPN and CD68 staining assay than the oscillatory shear stress region. The latter shows an apparently higher content of vascular smooth muscle cells (VSMC) and collagen, suggesting that the latter is prone to be stable plaques. Further oil red O staining reveals that the lowered shear stress region is rich in lipids and thus tends to be vulnerable. The quantitative data in Figure 5d clearly reveal that the expression of OPN in the low shear stress region is substantially higher than the oscillatory shear stress region, but the content of macrophages is just slightly higher for the lowered shear stress region, suggesting that the OPN expression level is a more favorable choice for accessing the vulnerability of atherosclerotic plaques than the total content of macrophages. Upconversion optical imaging based on UNCPS has been successfully applied for detecting tiny tumors as well as micrometastasis smaller than 1 mm in our previous studies,²⁰ especially two adjacent tumor lesions were successfully differentiated, indicating a great potential of the upconversion probes in ultrasensitive detections of small malignant lesions. The imaging results in Figure 5b reveal that the nanoprobe presents a higher affinity to the plaques that are upstream from the cast, *i.e.*, plaques with more vulnerable features. Although both phenotypes of plaques present detectable optical signals owing to the expression of OPN, the expression level starts to play a role in showing the vulnerable ones through prolonged observation. One should mention that the integrated signal intensity of the lower region is 4.1 times that of the upper region, which well coincides with the ratio of OPN expression levels between vulnerable and stable plaques in Figure 5d. The histological analysis suggests that the vulnerable and stable plaques can be distinguished by the OPN level, which thus supports the current strategy of detecting vulnerable plaques through OPN targeting.

In addition, MR imaging studies were also carried out with a parallel group of model mice to confirm the UCNP-anti-OPN probes for dual-modality imaging of atherosclerotic plaques. The results given in Figure 6 reveal that the lowered shear stress region presents relatively stronger T_1 signals than the oscillatory shear stress region. Although the plaques are very small, limited by the size of the carotid artery of mice, the MRI results suggest that the UCNP-anti-OPN probe can be used for detecting both vulnerable and stable plaques *in vivo*.

CONCLUSION

In summary, an OPN-specific upconversion luminescent probe (UCNP-anti-OPN) has been constructed, based on the conjugation between NaGdF₄:Yb,Er@NaGdF₄ nanoparticles and an OPN antibody, to detect vulnerable atherosclerotic plaques *in vivo*. The resulting UCNP-anti-OPN probe presents an excellent targeting ability for model foamy macrophages obtained upon Ox-LDL stimulation of macrophages and a remarkable binding specificity in comparison with unstimulated macrophages, which enables successful *in vivo* imaging of both vulnerable and stable atherosclerotic plaques through optical and MR imaging. Most importantly, the *ex vivo* immunohistochemical studies clearly reveal that OPN is strongly associated with the vulnerability of atherosclerotic plaques, which provides a possible way for differential diagnosis of atherosclerotic plaques *via* quantitative/semiquantitative detection of OPN expression through imaging.

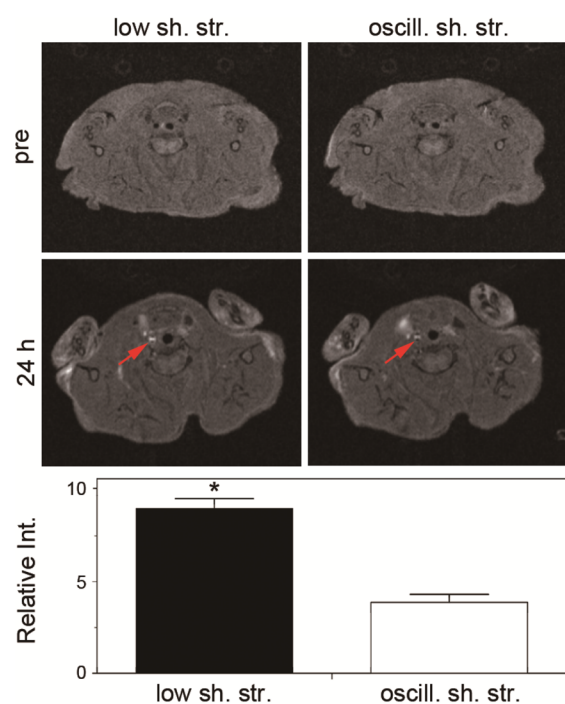


Figure 6. MR imaging of the vulnerable plaque (left) and stable plaque (right), as indicated by red arrows (top panel), and the relative T_1 signal intensities of the corresponding plaques recorded 24 h after the injection of UCNP-anti-OPN probes ($*P < 0.05$) (bottom panel).

METHODS

Animal Models of Stable and Vulnerable Atherosclerotic Plaques. Female 6-week-old C57 mice with a high fat diet (HFD) (containing 15% fat and 0.25% cholesterol) were purchased from Vital River, Beijing. ApoE^{-/-} mice were fed a high-fat diet (HFD) for 2 weeks before a rigid, polyether ketone perivascular cuff (Promolding, The Netherlands) was placed around the right common carotid artery, as previously reported.²⁹ Briefly, mice were anesthetized with 10% chloral hydrate (6 mL/kg), and the anterior cervical triangles were accessed by a sagittal anterior neck incision. The right common carotid artery was dissected from circumferential connective tissues. The cuff was placed around the right common carotid artery, the wounds were closed, and the animals were allowed to recover. Then the mice were kept on a HFD for another 16 weeks. All animal studies and procedures were performed according to a protocol approved by the Chinese PLA General Hospital Animal Care and Use Committee in accordance with the Care and Use of Laboratory Animals formulated by the National Society for Medical Research.

Reagents and Antibodies. The following materials were purchased from Sigma-Aldrich: GdCl₃·6H₂O, YbCl₃·6H₂O, ErCl₃·6H₂O, oleic acid (OA), 1-octadecene (ODE), ammonium fluoride (NH₄F), and tris(2-carboxyethyl) phosphine hydrochloride (TCEP). Analytical grade chemicals such as ethanol, cyclohexane, and tetrahydrofuran (THF) were purchased from Sinopharm Chemical Reagent Beijing, Co. Ltd. Mal-PEG-dp was a customized product provided by Beijing Oneder Hightech Co. Ltd.

RPMI 1640 culture medium and fetal bovine serum (FBS) were obtained from Gibco (Grand Island, NY, USA). Rabbit antimouse CD68 was purchased from Abcam (Cambridge, UK) (1:1000 for Western blot, 1:200 for immunohistochemical staining), rabbit antimouse OPN antibody and mIgG from Beijing Biosynthesis Biotechnology Co. Ltd., 3-(4,5-dimethyl-2-thiazolyl)-2,5-diphenyl-2-H-tetrazolium bromide (MTT) from Sigma-Aldrich (St Louis, MO, USA), *in situ* cell death detection kit, POD from Roche Diagnostics (Shanghai), and Raw 264.7 macrophages from Bo Gu Biology Technology (Shanghai) were used as received.

Preparation of NaGdF₄:Yb,Er Core Nanocrystals. NaGdF₄:Yb,Er core nanocrystals (12.4 nm) were synthesized according to our previous reports.^{20,26} Typically, GdCl₃·6H₂O (0.80 mmol), YbCl₃·6H₂O (0.18 mmol), and ErCl₃·6H₂O (0.02 mmol) were mixed with 14 mL of OA and 16 mL of ODE in a 100 mL flask. H₂O was removed by heating the resultant mixture to 150 °C under reduced pressure, and a homogeneous solution was formed. After the solution was cooled to 50 °C, 10 mL of methanol solution containing NaOH (2.5 mmol) and NH₄F (4 mmol) was slowly introduced, and the reaction system was then kept under stirring at 50 °C for 30 min. Subsequently, methanol in the system was removed by keeping the reaction system at 100 °C for 10 min under reduced pressure. Under atmospheric pressure, the finally formed reaction mixture was heated to 300 °C. The reactions were held for 1 h under nitrogen protection and then terminated by cooling the reaction mixture to room temperature. The resultant nanoparticles were precipitated by ethanol, collected by centrifugation, washed with ethanol for several cycles, and finally redispersed in cyclohexane for further experiments.

Preparation of Core@shell Structured NaGdF₄:Yb,Er@NaGdF₄ Nanocrystals. Typically, 5 mL of cyclohexane solution of the purified NaGdF₄:Yb,Er core nanocrystals was mixed with GdCl₃·6H₂O (0.50 mmol), 4 mL of OA, and 16 mL of ODE in a 100 mL flask. The growth of the NaGdF₄ shell and the following purification procedures for the core@shell particles were the same as those for the core nanocrystals, except 5 mL methanol solution containing NaOH (2.5 mmol), and NH₄F (4 mmol) was slowly introduced while the solution was cooled to 50 °C. The purified nanoparticles were also redispersed in cyclohexane for further experiments.

Ligand Exchange. Approximately 10 mg of the purified particles (NaGdF₄:Yb,Er or NaGdF₄:Yb,Er@NaGdF₄) and 100 mg of mal-PEG-dp were dissolved in 5 mL of THF. The ligand exchange reaction took place overnight at 40 °C. Then, the resulting PEGylated particles were precipitated by cyclohexane, washed with cyclohexane three times, and finally dried under vacuum at room temperature. The upconversion fluorescence emissions of the PEGylated core or core@shell nanoparticles in Milli-Q water were recorded by a fluorescence spectrometer equipped with a 980 nm laser with a fixed excitation power density.

Characterization of Core and Core@shell Nanocrystals. TEM images were obtained with a JEM-100CXII microscope operating at an accelerating voltage of 100 kV to characterize the particle size. The XRD patterns of the particle samples were recorded on a Rigaku D/Max-2500 diffractometer under Cu Kα₁ radiation ($\lambda = 1.54056 \text{ \AA}$). The concentration of the rare-earth elements in different nanoparticle samples was determined by using an inductively coupled plasma atomic emission spectrometer (Thermo Icap 6300) from PerkinElmer after the particles were eroded with concentrated nitric acid. The upconversion fluorescence spectra were recorded on a Cary Eclipse fluorescence spectrophotometer equipped with a 980 nm CW laser diode (2 W) serving as the excitation source.

Preparation of OPN-Specific Probe (UCNP-Anti-OPN). OPN antibody (4.6 mg/mL in 10 × PBS) was subjected to mild reduction by TCEP to convert the disulfide groups in the Fc fragments to thiol groups. The partially reduced mAb was purified by using 30 K MWCO centrifugal devices (Millipore YM-30). The UCNP-OPN probe was prepared by conjugating the partially reduced OPN antibody to (mal-PEG-dp)-coated core@shell nanoparticles in Tris-buffered saline (pH 7.04) through a “click” reaction. The molar ratio of antibody-to-particle was 4:1. The resulting UCNP-anti-OPN conjugates were transferred into 1 × PBS buffer and stored at 4 °C for further use. The formation of the conjugates was followed by dynamic light scattering at 298.0 K with Nano ZS (Malvern) equipped with a solid state He-Ne laser ($\lambda = 632.8 \text{ nm}$).

Cell Culture and *in Vitro* Cytotoxicity Assessment of UCNP-Anti-OPN Conjugates. Mouse macrophages line Raw 264.7 were cultured using RPMI 1640 supplemented with 15% FBS and maintained in a humidified environment containing 5% CO₂ and air at 37 °C. Terminal deoxy-nucleotidyl transferase-mediated dUTP nick end labeling (TUNEL) and flow cytometry assay were adopted to evaluate the cytotoxic effect of nanoparticles on macrophages. When

cells reached 90% surface coverage, sterile PBS was added, and the cells were removed by gently rinsing. For cells' apoptosis assessment, cells preconditioned with nanoparticles (0, 30 $\mu\text{g}/\text{mL}$) for 24 h were collected for TUNEL apoptosis assay using an *in situ* cell death detection kit according to the manufacturer's instructions. DAPI staining was performed for total nuclei quantification. The TUNEL-positive cells were imaged by a confocal fluorescence microscope (Olympus FV 10i, Japan).

For further quantitative analysis of cell apoptosis, 5×10^5 cells with treatment of different concentrations of nanoparticles (0, 10, 30 $\mu\text{g}/\text{mL}$) were harvested and washed with PBS and then stained with propidium iodide (PI) and Annexin V-FITC (BD Pharmingen). The data were analyzed by flow cytometry (BD FACSAria, USA) with CellQuest research software.

In Vitro Cellular Imaging. Raw 264.7 cells were seeded on a Nunc Lab-Tek II 8-well chamber slide system, and macrophage-derived foam cells were stimulated by Ox-LDL (50 $\mu\text{g}/\text{mL}$) for 24 h and then incubated with UCNP-anti-OPN for another 8 h. Blocking groups were incubated with excess anti-OPN antibody and UCNP-anti-OPN probes simultaneously. Subsequently, the cells were rinsed three times with Milli-Q water to remove the unbound probes and fixed in 4% paraformaldehyde for 20 min. The resulting cells were further incubated with 5 $\mu\text{g}/\text{mL}$ Hoechst 33258 for nuclei staining. Fluorescence imaging was conducted on an Olympus FV1200 equipped with a 980 nm laser as excitation source. Green emission and red emission channels were defined with optical windows of 520–560 nm and 575–675 nm, respectively.

In Vivo Upconversion Luminescence Imaging. UCNP-anti-OPN probes were injected into ApoE^{-/-} mice ($n = 4$) *via* tail vein with a dose of 15 mg Gd per kg body weight of the mice. The upconversion luminescence images of the atherosclerotic plaques were captured with a cooled electron-multiplying charge-coupled device (iXon, 888Andor) equipped with a 400–750 nm band-pass filter set (AZURE Photonics Co., Ltd.). A 0–30 W adjustable CW 980 nm laser (Hi-Tech Optoelectronics Co., Ltd.) with a beam size of 20 mm was used as an excitation source. The excitation light density was approximately 320 mW/cm². The distance between the skin on top of the neck and the laser diode was approximately 40 mm. The luminescent images were superimposed on bright-field images with Matlab.

In Vivo MR Imaging. T₁-weighted images ApoE^{-/-} mice ($n = 3$) were acquired on a 7-T Bruker using a fast gradient echo FLASH sequence with the following parameters: TE = 1.86 ms; TR = 150 ms; NEX = 5.0; FA = 80°, MTX = 256 × 256; FOV = 35 × 35 mm; slide thickness = 1 mm; and a spin echo T₁-RARE sequence with the following parameters: TE = 6.17 ms; TR = 330 ms; NEX = 5.5; FA = 90°; MTX = 256 × 256, FOV = 35 × 35 mm; slide thickness = 1 mm.

Immunohistochemistry and Pathological Analysis. To verify the animal model of atherosclerosis, the carotid artery of mice was harvested, embedded in 4% formaldehyde for 20 min, and then stained with oil red dye. After being washed with 60% isopropanol, microscopy images were taken. Immunohistochemistry staining was performed to further analyze the histology and the expression of OPN in the atherosclerotic plaques. Briefly, an artery with plaques was embedded in tissue freezing medium and snap-frozen. Transverse cryosections (10 μm thick) were collected, fixed in cold acetone, and stained with CD68, oil red O, collagen, and OPN antibody and DAPI for nuclei, respectively. Microscopic images were taken with an inverted microscope (Olympus, Japan).

Statistics Analysis. Continuous variables were presented as mean \pm standard deviation (SD), and the multigroup comparisons were made with a one-way factor analysis of variance, followed by Dunnett's post hoc test. Data expressed as proportions were assessed with a chi square test. Values of $P < 0.05$ were considered to indicate a statistically significant difference. GraphPad Prism-5 statistic software (La Jolla, CA) was used for all data analysis.

AUTHOR INFORMATION

Corresponding Authors

*E-mail: gaomy@iccas.ac.cn.

*E-mail: wind8828@gmail.com.

ORCID

Mingyuan Gao: 0000-0002-7360-3684

Author Contributions

[†]These authors contributed equally to this work.

Notes

The authors declare no competing financial interest.

ACKNOWLEDGMENTS

The authors are grateful to Ping Guo and Jianfeng Zeng from the School of Radiation Medicine and Protection Medical College of Soochow University for their great help with the confocal microscopy experiments. This work was financially supported by the National Natural Science Foundation of China (81571746, 81325009, 81530057, 81530058).

REFERENCES

- (1) Go, A. S.; Mozaffarian, D.; Roger, V. L.; Benjamin, E. J.; Berry, J. D.; Baha, M. J.; Dai, S. F.; Ford, E. S.; Fox, C. S.; Franco, S.; Fullerton, H. J.; Gillespie, C.; Hailpern, S. M.; Heit, J. A.; Howard, V. J.; Huffman, M. D.; Judd, S. E.; Kissela, B. M.; Kittner, S. J.; Lackland, D. T.; et al. Heart Disease and Stroke Statistics-2014 Update A Report From the American Heart Association. *Circulation* **2014**, *129*, E28–E292.
- (2) Chung, E. J.; Tirrell, M. Recent Advances in Targeted, Self-Assembling Nanoparticles to Address Vascular Damage Due to Atherosclerosis. *Adv. Healthcare Mater.* **2015**, *4*, 2408–2422.
- (3) World Health Organization. *Global Status Report on Non-communicable Diseases 2010*; World Health Organization: Geneva, 2011.
- (4) Amirbekian, V.; Lipinski, M. J.; Briley-Saebo, K. C.; Amirbekian, S.; Aguinaldo, J. G. S.; Weinreb, D. B.; Vucic, E.; Frias, J. C.; Hyafil, F.; Mani, V.; Fisher, E. A.; Fayad, Z. A. Detecting and Assessing Macrophages *in vivo* to Evaluate Atherosclerosis Noninvasively Using Molecular MRI. *Proc. Natl. Acad. Sci. U. S. A.* **2007**, *104*, 961–966.
- (5) Dweck, M. R.; Aikawa, E.; Newby, D. E.; Tarkin, J. M.; Rudd, J. H. F.; Narula, J.; Fayad, Z. A. Noninvasive Molecular Imaging of Disease Activity in Atherosclerosis. *Circ. Res.* **2016**, *119*, 330–340.
- (6) Kolodgie, F. D.; Gold, H. K.; Burke, A. P.; Fowler, D. R.; Kruth, H. S.; Weber, D. K.; Farb, A.; Guerrero, L. J.; Hayase, M.; Kutys, R.; Narula, J.; Finn, A. V.; Virmani, R. Intraplaque Hemorrhage and Progression of Coronary Atheroma. *N. Engl. J. Med.* **2003**, *349*, 2316–2325.
- (7) Virmani, R.; Burke, A. P.; Farb, A.; Kolodgie, F. D. Pathology of the Vulnerable Plaque. *J. Am. Coll. Cardiol.* **2006**, *47*, C13–C18.
- (8) MacNeill, B. D.; Jang, I. K.; Bouma, B. E.; Iftimia, N.; Takano, M.; Yabushita, H.; Shishkov, M.; Tearney, G. J. *In vivo* Macrophage Imaging of Acute Coronary Syndromes with Intracoronary Optical Coherence Tomography. *J. Am. Coll. Cardiol.* **2004**, *43*, A33.
- (9) Tarkin, J. M.; Dweck, M. R.; Evans, N. R.; Takx, R. A. P.; Brown, A. J.; Tawakol, A.; Fayad, Z. A.; Rudd, J. H. F. Imaging Atherosclerosis. *Circ. Res.* **2016**, *118*, 750–769.
- (10) Miao, Q. Q.; Lyu, Y.; Ding, D.; Pu, K. Y. Semiconducting Oligomer Nanoparticles as an Activatable Photoacoustic Probe with Amplified Brightness for *in vivo* Imaging of pH. *Adv. Mater.* **2016**, *28*, 3662–3668.
- (11) Weissleder, R.; Nahrendorf, M.; Pittet, M. J. Imaging Macrophages with Nanoparticles. *Nat. Mater.* **2014**, *13*, 125–138.
- (12) McAteer, M. A.; Mankia, K.; Ruparella, N.; Jefferson, A.; Nugent, H. B.; Stork, L. A.; Channon, K. M.; Schneider, J. E.; Choudhury, R. P. A Leukocyte-Mimetic Magnetic Resonance Imaging Contrast Agent Homes Rapidly to Activated Endothelium and Tracks

with Atherosclerotic Lesion Macrophage Content. *Arterioscler., Thromb., Vasc. Biol.* **2012**, *32*, 1427–1435.

(13) Lobatto, M. E.; Fuster, V.; Fayad, Z. A.; Mulder, W. J. M. Perspectives and Opportunities for Nanomedicine in the Management of Atherosclerosis. *Nat. Rev. Drug Discovery* **2011**, *10*, 835–852.

(14) Nahrendorf, M.; Waterman, P.; Thurber, G.; Groves, K.; Rajopadhye, M.; Panizzi, P.; Marinelli, B.; Aikawa, E.; Pittet, M. J.; Swirski, F. K.; Weissleder, R. Hybrid *in vivo* FMT-CT Imaging of Protease Activity in Atherosclerosis with Customized Nanosensors. *Arterioscler., Thromb., Vasc. Biol.* **2009**, *29*, 1444–U89.

(15) Winter, P. M.; Morawski, A. M.; Caruthers, S. D.; Fuhrhop, R. W.; Zhang, H. Y.; Williams, T. A.; Allen, J. S.; Lacy, E. K.; Robertson, J. D.; Lanza, G. M.; Wickline, S. A. Molecular Imaging of Angiogenesis in Early-stage Atherosclerosis with $\alpha(v)\beta(3)$ -Integrin-targeted Nanoparticles. *Circulation* **2003**, *108*, 2270–2274.

(16) Richards, J. M. J.; Semple, S. I.; MacGillivray, T. J.; Gray, C.; Langrish, J. P.; Williams, M.; Dweck, M.; Wallace, W.; McKillop, G.; Chalmers, R. T. A.; Garden, O. J.; Newby, D. E. Abdominal Aortic Aneurysm Growth Predicted by Uptake of Ultrasmall Superparamagnetic Particles of Iron Oxide a Pilot Study. *Circ. Cardiovasc. Imaging* **2011**, *4*, 274–281.

(17) Tang, T. Y.; Howarth, S. P. S.; Miller, S. R.; Graves, M. J.; Patterson, A. J.; U-King-Im, J. M.; Li, Z. Y.; Walsh, S. R.; Brown, A. P.; Kirkpatrick, P. J.; Warburton, E. A.; Hayes, P. D.; Varty, K.; Boyle, J. R.; Gaunt, M. E.; Zalewski, A.; Gillard, J. H. The ATHEROMA (Atorvastatin Therapy: Effects on Reduction of Macrophage Activity) Study Evaluation Using Ultrasmall Superparamagnetic Iron Oxide-Enhanced Magnetic Resonance Imaging in Carotid Disease. *J. Am. Coll. Cardiol.* **2009**, *53*, 2039–2050.

(18) Kooi, M. E.; Cappendijk, V. C.; Cleutjens, K. B. J. M.; Kessels, A. G. H.; Kitslaar, P. J. E. H. M.; Borgers, M.; Frederik, P. M.; Daemen, M. J. A. P.; van Engelsehoven, J. M. A. Accumulation of Ultrasmall Superparamagnetic Particles of Iron Oxide in Human Atherosclerotic Plaques Can Be Detected by *in vivo* Magnetic Resonance Imaging. *Circulation* **2003**, *107*, 2453–2458.

(19) Quillard, T.; Croce, K.; Jaffer, F. A.; Weissleder, R.; Libby, P. Molecular Imaging of Macrophage Protease Activity in Cardiovascular Inflammation *in vivo*. *Thromb. Haemostasis* **2011**, *105*, 828–836.

(20) Qiao, R. R.; Liu, C. H.; Liu, M. H.; Hu, H.; Liu, C. Y.; Hou, Y.; Wu, K. C.; Lin, Y. N.; Liang, J. M.; Gao, M. Y. Ultrasensitive *in vivo* Detection of Primary Gastric Tumor and Lymphatic Metastasis Using Upconversion Nanoparticles. *ACS Nano* **2015**, *9*, 2120–2129.

(21) Liu, C.; Hou, Y.; Gao, M. Are Rare-Earth Nanoparticles Suitable for *in vivo* Applications? *Adv. Mater.* **2014**, *26*, 6922–6932.

(22) Fan, W. P.; Bu, W. B.; Shi, J. L. On the Latest Three-Stage Development of Nanomedicines Based on Upconversion Nanoparticles. *Adv. Mater.* **2016**, *28*, 3987–4011.

(23) Chen, G. Y.; Qiu, H. L.; Prasad, P. N.; Chen, X. Y. Upconversion Nanoparticles: Design, Nanochemistry, and Applications in Theranostics. *Chem. Rev.* **2014**, *114*, 5161–5214.

(24) Zhang, F.; Shi, Q. H.; Zhang, Y. C.; Shi, Y. F.; Ding, K. L.; Zhao, D. Y.; Stucky, G. D. Fluorescence Upconversion Microbarcodes for Multiplexed Biological Detection: Nucleic Acid Encoding. *Adv. Mater.* **2011**, *23*, 3775–3779.

(25) Xu, C. T.; Svenmarker, P.; Liu, H. C.; Wu, X.; Messing, M. E.; Wallenberg, L. R.; Andersson-Engels, S. High-Resolution Fluorescence Diffuse Optical Tomography Developed with Nonlinear Upconverting Nanoparticles. *ACS Nano* **2012**, *6*, 4788–4795.

(26) Liu, C. Y.; Gao, Z. Y.; Zeng, J. F.; Hou, Y.; Fang, F.; Li, Y. L.; Qiao, R. R.; Shen, L.; Lei, H.; Yang, W. S.; Gao, M. Y. Magnetic/Upconversion Fluorescent NaGdF₄:Yb,Er Nanoparticle-Based Dual-Modal Molecular Probes for Imaging Tiny Tumors *in vivo*. *ACS Nano* **2013**, *7*, 7227–7240.

(27) Hudson, D. E.; Hudson, D. O.; Wininger, J. M.; Richardson, B. D. Penetration of Laser Light at 808 and 980nm in Bovine Tissue Samples. *Photomed. Laser Surg.* **2013**, *31*, 163–168.

(28) Scatena, M.; Liaw, L.; Giachelli, C. M. Osteopontin - A Multifunctional Molecule Regulating Chronic Inflammation and

Vascular Disease. *Arterioscler., Thromb., Vasc. Biol.* **2007**, *27*, 2302–2309.

(29) Matsui, Y.; Okamoto, H.; Inobe, M.; Nan, J.; Sugawara, T.; Kon, S.; Uede, T. Osteopontin Deficiency Attenuates Atherosclerosis in Female Apolipoprotein E Deficient Mice. *Circulation* **2003**, *23*, 1029–1034.

(30) Cheng, C.; Tempel, D.; van Haperen, R.; van der Baan, A.; Grosveld, F.; Daemen, M. J. A. P.; Krams, R.; de Crom, R. Atherosclerotic Lesion Size and Vulnerability Are Determined by Patterns of Fluid Shear Stress. *Circulation* **2006**, *113*, 2744–2753.

(31) Boyer, J. C.; Manseau, M. P.; Murray, J. I.; van Veggel, F. C. J. M. Surface Modification of Upconverting NaYF₄ Nanoparticles with PEG-Phosphate Ligands for NIR (800 nm) Bioluminescence within the Biological Window. *Langmuir* **2010**, *26*, 1157–1164.

(32) Chen, D. Q.; Huang, P. Highly Intense Upconversion Luminescence in Yb/Er:NaGdF₄@NaYF₄ Core-Shell Nanocrystals with Complete Shell Enclosure of the Core. *Dalton Trans.* **2014**, *43*, 11299–11304.

(33) O'Brien, E. R.; Garvin, M. R.; Stewart, D. K.; Hinohara, T.; Simpson, J. B.; Schwartz, S. M.; Giachelli, C. M. Osteopontin Is Synthesized by Macrophage, Smooth-Muscle, and Endothelial-Cells in Primary and Restenotic Human Coronary Atherosclerotic Plaques. *Arterioscler., Thromb., Vasc. Biol.* **1994**, *14*, 1648–1656.

(34) Bidder, M.; Shao, J. S.; Charlton-Kachigian, N.; Loewy, A. P.; Semenkovich, C. F.; Towler, D. A. Osteopontin Transcription in Aortic Vascular Smooth Muscle Cells Is Controlled by Glucose-Regulated Upstream Stimulatory Factor and Activator Protein-1 Activities. *J. Biol. Chem.* **2002**, *277*, 44485–44496.

(35) Giachelli, C. M.; Lombardi, D.; Johnson, R. J.; Murry, C. E.; Almeida, M. Evidence for a Role of Osteopontin in Macrophage Infiltration in Response to Pathological Stimuli *in vivo*. *Am. J. Pathol.* **1998**, *152*, 353–358.

(36) Qiao, H.; Wang, Y.; Zhang, R.; Gao, Q.; Liang, X.; Gao, L.; Jiang, Z.; Qiao, R.; Han, D.; Zhang, Y.; Qiu, Y.; Tian, J.; Gao, M.; Cao, F. MRI/Optical Dual-Modality Imaging of Vulnerable Atherosclerotic Plaque with an Osteopontin-Targeted Probe Based on Fe₃O₄ Nanoparticles. *Biomaterials* **2017**, *112*, 336–345.

(37) Lee, T. S.; Lu, K. Y.; Yu, Y. B.; Lee, H. T.; Tsai, F. C. β Common Receptor Mediates Erythropoietin-Conferred Protection on OxLDL-Induced Lipid Accumulation and Inflammation in Macrophages. *Mediators Inflammation* **2015**, *2015*, 1–13.

(38) Melzer, S.; Ankri, R.; Fixler, D.; Tarnok, A. Nanoparticle Uptake by Macrophages in Vulnerable Plaques for Atherosclerosis Diagnosis. *J. Biophotonics* **2015**, *8*, 871–883.

(39) Lipinski, M. J.; Amirbekian, V.; Frias, J. C.; Aguinaldo, J. G. S.; Mani, V.; Briley-Saebo, K. C.; Fuster, V.; Fallon, J. T.; Fisher, E. A.; Fayad, Z. A. MRI to Detect Atherosclerosis with Gadolinium-Containing Immunomicelles Targeting the Macrophage Scavenger Receptor. *Magn. Reson. Med.* **2006**, *56*, 601–610.

(40) Morishige, K.; Kacher, D. F.; Libby, P.; Josephson, L.; Ganz, P.; Weissleder, R.; Aikawa, M. High-Resolution Magnetic Resonance Imaging Enhanced With Superparamagnetic Nanoparticles Measures Macrophage Burden in Atherosclerosis. *Circulation* **2010**, *122*, 1707–1715.

(41) Trivedi, R. A.; Mallawarachi, C.; U-King-Im, J. M.; Graves, M. J.; Horsley, J.; Goddard, M. J.; Brown, A.; Wang, L. Q.; Kirkpatrick, P. J.; Brown, J.; Gillard, J. H. Identifying Inflamed Carotid Plaques Using *in vivo* USPIO-enhanced MR Imaging to Label Plaque Macrophages. *Arterioscler., Thromb., Vasc. Biol.* **2006**, *26*, 1601–1606.

(42) Wentzel, J. J.; Kloet, J.; Andhyiswara, I.; Oomen, J. A. F.; Schuurbers, J. C. H.; de Smet, B. J. G. L.; Post, M. J.; de Kleijn, D.; Pasterkamp, G.; Borst, C.; Slager, C. J.; Krams, R. Shear-Stress and Wall-Stress Regulation of Vascular Remodeling After Balloon Angioplasty - Effect of Matrix Metalloproteinase Inhibition. *Circulation* **2001**, *104*, 91–96.

(43) Oyre, S.; Hansen, M. S.; Flaagoy, H.; Ringgaard, S.; Erlandsen, M.; Pedersen, E. M. A Noninvasive User-Independent Method for Determination of Lumen Vessel Area and Wall Shear Stress Using

MRI; Preliminary Application For Vascular Function in the Brachial and Coronary Arteries. *Circulation* **1999**, *100*, 457–457.